Chemical Geology 367 (2014) 70–82

Contents lists available at ScienceDirect

Chemical Geology

journal homepage: www.elsevier.com/locate/chemgeo

Crystal growth rate effect on Mg/Ca and Sr/Ca partitioning between calcite and fluid: An in situ approach

R.I. Gabitov [a,*], A. Sadekov [b], A. Leinweber [c]

[a] Mississippi State University, MS 39762-5448, USA
[b] University of Cambridge, Cambridge CB23EQ, UK
[c] University of California, Los Angeles, CA 90095, USA

ARTICLE INFO

Article history:
Received 16 May 2013
Received in revised form 27 December 2013
Accepted 29 December 2013
Available online 10 January 2014

Editor: J. Fein

Keywords:
Calcite
Magnesium
Strontium
Growth rate
SIMS
Equilibrium

ABSTRACT

Partition coefficients of Mg and Sr (K^{Mg} and K^{Sr}) between calcite and fluid were determined in crystals grown under different rates (V), where V is defined as the crystal extension per unit of time (nm/s). Addition of rare earth elements (REE) into the fluid, leads to REE preservation in the calcite. This preservation allows for a direct determination of the values of V by measuring the widths of the REE spiked zones. The edge to edge spot analyses of Mg/Ca, Sr/Ca, and REE/Ca in the individual crystals were conducted using Secondary Ion Mass Spectrometry (SIMS). The Mg/Ca and Sr/Ca ratios in the fluids, from which calcites precipitated, were also measured with Inductively Coupled Plasma Atomic Emission Spectroscopy (ICP-OES). This allowed for the first time, to evaluate K^{Mg} in situ in the individual crystals without averaging the data from the multiple calcite crystals. Results show that K^{Sr} increases by a factor of six with increasing calcite growth rate from 0.001 to 4 nm/s. K^{Mg} decreases by a factor of three with the same increase of V values. These K^{Sr} and K^{Mg} behaviors were described quantitatively using a growth entrapment model (GEM). According to the GEM simulations, Sr is enriched and Mg is depleted in the near-surface layer of calcite relative to the bulk lattice. This distinct outermost region of the crystal may be fully or partially captured by its lattice during rapid growth. This process causes disequilibrium partitioning of Sr and Mg through growth entrapment.

1. Introduction

Mg/Ca and Sr/Ca composition (metal to calcium ratio Me/Ca) of the calcite in speleothems, foraminifera, coccolithophores, and mollusks has been widely used as proxies for paleoenviromental studies during the last two decades (e.g. McCorkle et al., 1995; Elderfield et al., 1996; Rosenthal et al., 1997; Lea et al., 1999; Martin et al., 1999; Stoll and Schrag, 2000; Dekens et al., 2002; Elderfield et al., 2002; Rickaby et al., 2002; Stoll et al., 2002a,b; Eggins et al., 2004; Rosenthal et al., 2004; Bentov and Erez, 2005; Bice et al., 2005; Immenhauser et al., 2005; Mortyn et al., 2005; Sadekov et al., 2005; Cruz et al., 2007; Cleroux et al., 2008; Freitas et al., 2008, 2009; Filipsson et al., 2010; Griffiths et al., 2010; Sadekov et al., 2010). The high sensitivity of Mg/Ca and Sr/Ca values relative to the temperature at which calcite precipitates, provides a unique geochemical tool in studying paleoclimate. However, the inconsistency between different Me/Ca-temperature calibrations suggests that Mg/Ca and Sr/Ca incorporation into calcite is not solely controlled by temperature or composition of the growth environment (Lea et al., 1999; Dekens et al., 2002; Cleroux et al., 2008, etc.). In addition, in situ electron microprobe, Nano-SIMS, and Scanning Transmission X-ray Microscope imaging reveal heterogeneous distribution of Me/Ca values within biogenic calcite, which is yet to be explained using known calcification models (Erez, 2003; Eggins et al., 2004; Bentov and Erez, 2005; Sadekov et al., 2005; Bentov and Erez, 2006; Kunioka et al., 2006; Branson et al., 2013). Therefore, better understanding of the processes affecting trace metal incorporation is required in order to improve the use of Me/Ca as paleoclimate proxies.

Until recently, the majority of research on how solution chemistry and precipitation rate (amount of crystallized calcite per area and time) affects inorganic calcite composition has been conducted using bulk analytical techniques (Holland et al., 1964; Lorens, 1981; Mucci and Morse, 1983; Tesoriero and Pankow, 1996; Tang et al., 2008, 2012, etc.). However, intra-crystalline variability remained largely unknown in the aforementioned studies. In situ works on Sr and Mg incorporation into vicinal calcite faces, grown at different step velocities, provide the compositional (Mg and Sr), but not the partition (K^{Mg} and K^{Sr}) information (Paquette and Reeder, 1995; Wasylenki et al., 2005, etc.). In order to fill this gap, we utilize a different technique that results in robust, in situ K^{Me} data as a function of the calcite growth rate. Our approach provides the values of K^{Me}, which is defined as $(Me/Ca)_{calcite}/(Me/Ca)_{fluid}$, where Me corresponds to Mg or Sr. This method allows tracking of potential changes in calcification rates during crystal formation resulting in the intra-crystalline variability (e.g. K^{Mg} is the highest at the crystal edges). This approach builds on the method described in Gabitov and Watson (2006); with additional sequentially spiking calcite-

* Corresponding author.
E-mail address: rinat.gabitov@gmail.com (R.I. Gabitov).

0009-2541/$ – see front matter © 2014 Elsevier B.V. All rights reserved.
http://dx.doi.org/10.1016/j.chemgeo.2013.12.019

precipitating fluids with REE dopants (see Gabitov et al., 2012). SIMS analyses of calcite crystals yielded REE patterns resulting in evaluation of crystal growth rates. This technique allows for the determination of relationships between K^{Me} and extension rates of exactly the same crystals, which were examined with optical and scanning electron microscopy. Therefore, the potential influence of solid or fluid inclusions is eliminated at the spatial resolution of a few microns. To our knowledge, this is the first study where K^{Mg} between calcite and fluid was determined in situ (using beam technique), without the averaging of Mg/Ca data from whole individual crystal or bulk calcite as performed by e.g. Mucci and Morse (1983), Huang and Fairchild (2001), Saulnier et al. (2012), Mavromatis et al. (2013). Our data provides unique insights regarding the chemical behavior of growing crystals; hence are potentially relevant to naturally occurring carbonates, because laboratory growth rates (0.001–5 nm/s) overlap with those of stalagmites, coccolithophores, foraminifera, and mollusks (0.001–3.3 nm/s) (ter Kuile and Erez, 1984; Baker et al., 1998; Owen et al., 2002; Stoll et al., 2002b; Freitas et al., 2009).

1.1. Influence of calcification rate on Me/Ca values calcite

Inorganic experiments showed that K^{Sr} strongly depends on calcite growth (V in distance per time, nm/s) and precipitation rates (R in mole per area per time, mol/m^2/s) (Lorens, 1981; Mucci and Morse, 1983; Tesoriero and Pankow, 1996; Gabitov and Watson, 2006; Nehrke et al., 2007; Tang et al., 2008, 2012). In addition, experiments using cultured coccolithophores showed an increase in Sr/Ca with increasing calcification rates defined as pg calcite/cell/day (Stoll et al., 2002a,b). The effect of precipitation rate on K^{Mg} is not as obvious as that on K^{Sr}, i.e. experimental data of Mavromatis et al. (2013) yielded an increase of K^{Mg} with calcite precipitation rate, but no effect of R on K^{Mg} was found in synthetic and foraminiferal calcite in the studies of Mucci and Morse (1983) and Nurnberg et al. (1996). Despite this controversy, Mg/Ca extensively varies within an individual foraminifera shell or in calcite crystals grown at relatively stable temperatures and fluid compositions (Reeder and Grams, 1987; Paquette and Reeder, 1995; Bentov and Erez, 2005; Sadekov et al., 2005; Wasylenki et al., 2005; Kunioka et al., 2006; Stephenson et al., 2008). In situ analyses yielded, unlike strontium, magnesium is enriched in the slower grown faces of the calcite precipitated from unstirred solutions (Paquette and Reeder, 1995). Wasylenki et al. (2005) observed similar Mg behavior when calcite precipitated from moderate stirred fluids; the vigorous stirring promoted Mg incorporation into faster grown faces of calcite. In the present study, unstirred fluid promoted growth of large calcite crystals. Solutions were agitated each time when REE spike was introduced.

2. Experimental and analytical methods

2.1. Calcite precipitation

The initial solution was prepared by dissolving NH_4Cl in deionized (DI) H_2O to the concentration of 0.5 mol/L, along with minor amounts of reagent grade $CaCl_2 \cdot 2H_2O$ (0.01), $MgCl_2 \cdot 6H_2O$ (10^{-3}), $SrCl_2 \cdot 6H_2O$ (10^{-4}), $BaCl_2 \cdot 2H_2O$ ($2 \cdot 10^{-5}$), $LiOH \cdot H_2O$ ($5 \cdot 10^{-4}$), H_3BO_3 (0.01), and U ICP-MS standard (10^{-5}) [values in parentheses are estimated concentrations in mol/L]. Initial Mg/Ca in our fluids (0.1 mol/mol) is significantly lower than that in seawater (5 mol/mol) because no calcite is expected to precipitate at $Mg/Ca_{fluid} \geq 0.25$ at 25 °C (Morse et al., 1997). Salinity of the fluid (29.4‰) was calculated from concentrations of the salts. The pH of solution was adjusted to 5.5 by addition of NaOH moreover the solution was used as a starting fluid in all experiments for consistency with the experiments of Paquette and Reeder (1995). The calcite growth method is based on the work of Gruzensky (1967) and modified with respect to sub-sampling and adding multiple REE spikes to the fluid. Calcite crystals precipitated from the Ca bearing solution of NH_4Cl in response to the diffusive flux of CO_2 from decomposition of ammonium carbonate [$(NH_4)_2CO_3$] at atmospheric pressure and constant temperatures of 19.7 ± 0.25, 21.7 ± 0.10, and 24.6 ± 0.10 °C (Fig. 1). Those three experiments will further be referred to as DSC-4, DC-3, and DC-1. We investigated the crystal growth rates under slow and fast growing conditions. Crystals grew in one 2 L Pyrex glass beaker in the slow calcite growth run DC-1. Polypropylene containers of 1 L were used in the fast calcite growth runs DC-3 and DSC-4. The crystal growth rate was controlled by the size of the opening in the container lid (small opening in DC-1 (<1 cm) and larger openings (>5 cm) in DC-3 and DSC-4). Truncated pyramid shaped calcite crystals grew outward from the bottom and the walls of the container, thus serving as substrates. Only a small fraction of the crystals precipitated at the fluid–gas interface. Once the first crystals became visible with the naked eye, 1 mL of Sm spiked H_2O was added to the fluid using a syringe attached to a piece of tubing, which was immersed into the calcite growth medium. The solution was homogenized in Sm by withdrawal and injection of 60 mL volume three times. An independent test with 1 mL of dye showed that this procedure is sufficient in achieving complete fluid homogenization. It was observed that the dye became homogenously distributed in minutes while crystal deposition occurred over periods of days.

La, Nd, Tb, and Pr spikes were introduced into the solution in a process similar to the aforementioned procedure after 24, 36, 86, and 129 days (t_{REE}) respectively, counting time from the addition of Sm ($t_{Sm} = 0$). The estimated concentration of REE in the growth medium ranged from 0.1 to 0.5 ppb. A few minutes prior to each REE addition, 5 mL of fluid was sampled for pH, which was measured using a OAKTON pH 510 m with "All-in-One" pH/Temp electrode calibrated with 7.00 and 10.00 pH buffers at NBS-scale. Additional samples of 190 mL were collected, filtered with 0.2 μm surfactant-free cellulose acetate membrane (Nalge Nunc International), poured into Nalgene bottles, and stored in a refrigerator at 2 °C to preclude further precipitation of calcite. The final remaining fluid was treated the same way as Nd and Tb sub-samples. At the time when Sm spike was injected, the pH of the fluid was 8.00 and it slowly increased during calcite crystallization to a pH of 8.19 (run DC-1) at the end of the slow growth experiment (Fig. S-1). The pH of the fluid at the onset of crystallization was estimated to be 7.96 ± 0.06, which is the average of pH values at t =

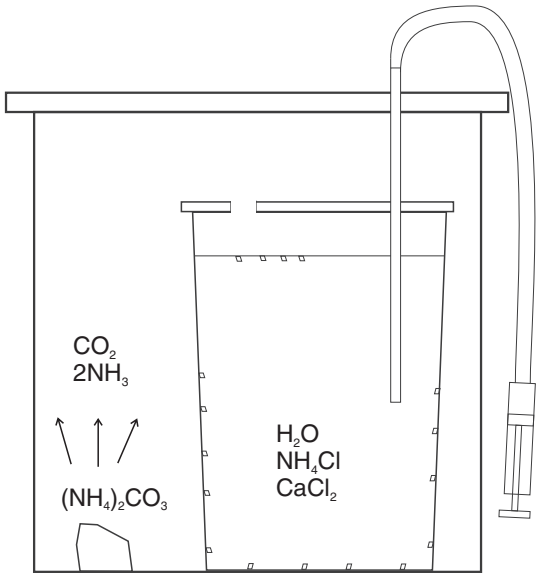

Fig. 1. Schematic of the calcite precipitation apparatus. Here, the outer plastic container holds elevated CO_2 and NH_3, which diffuses into the gas space above the Ca-bearing fluid in the inner polypropylene (or Pyrex glass) container, through the opening in the lid. Further diffusion into the fluid elevates the saturation state and promotes calcite precipitation.

−8 and t = 0 days (t is based on the visual observation of crystal appearance). At the time of Sm addition, the pH in the fast growth experiments (DC-3 and DSC-4) was 7.83 and 7.85 and then increased to 8.15 at the end of the runs. Crystals were extracted from the beakers using a spatula, rinsed twice with DI H_2O and once with methanol, dried at 40 °C, and then stored in a desiccator.

2.2. Analyses of fluids

2.2.1. Mg, Ca, and Sr analyses by ICP-OES

Trace metal analyses of the precipitation fluid were done using ICP-OES (*Varian VISTA PRO*™) at the School of GeoSciences, University of Edinburgh. The ICP-OES was configured using the standard protocol (de Villiers et al., 2002) for trace metal analyses in biogenic carbonates to obtain the best precision for Me/Ca measurements. The following settings are used to run the ICP-OES: coil power 1.2 kW; Plasma flow 15 L/min; Auxiliary flow 1.5 L/min; Nebulizer flow 0.8 L/min. Samples were introduced at a rate of 420 μL/min using MicroMist nebulizer and Cinnabar Cyclonic spray chamber (*Glass Expansion*™). To minimize the matrix effect of high concentrations of Ca and Na on Me/Ca values, we adopted the methods of de Villiers et al. (2002) and Greaves et al. (2005), which are commonly used for precise measurement of Mg/Ca and Sr/Ca values in biogenic calcite.

Each sample was measured in two steps: the first step was designed to measure Ca concentrations of a sample, and the second to accurately measure Me/Ca ratios of the samples. Ca concentrations were measured in 1/10 dilution of each sample, which were regressed against a set of Ca standards prepared gravimetrically from single element ICP-MS standard solution (*VWR Prolabo*™). After the first step, each sample was diluted to 15 ppm Ca concentration and run against a set of Sr/Ca and Mg/Ca standards, which have 15 ppm of Ca and a range of trace metal concentrations (e.g. Sr and Mg). These Sr/Ca and Mg/Ca standards were prepared gravimetrically from single element ICP-MS standard solutions (*VWR Prolabo*™) and used for routine measurements of trace metals in biogenic carbonates at the School of Geoscience, University of Edinburgh.

To monitor the stability of the ICP-OES, we analyzed JCp-1 (Hathorne et al., 2013) and ECRM 752-1 (Greaves et al., 2008), matrix matching reference materials every fifth sample. External errors were estimated at 1% 1 s.d. for ratio measurement and 2–5% for Ca concentrations. Internal (within day) reproducibility of the reference material ranges from 0.3% 1 s.d. for Sr/Ca and 0.2% 1 s.d. for Mg/Ca.

2.2.2. Analyses of dissolved inorganic carbon

Dissolved inorganic carbon (DIC) was determined using the coulometric SOMMA (Single-Operator Multi-Metabolic Analyzer) system at UCLA (for details see Johnson et al., 1993). The SOMMA is a system used to extract CO_2 out of a known amount of seawater. It is interfaced with a personal computer and coupled to a CO_2 coulometric detector (model 5011, supplied by UIC Coulometric Inc.). Pure CO_2 gas and DIC reference samples (Certified Reference Material, CRMs, produced by Andrew Dickson, Scripps Institution of Oceanography) are used to calibrate the measurements. The analytical precision of the DIC measurements was determined to be better than 0.8 μmol/kg and 149 comparisons with the CRMs indicate an accuracy of the method of better than ± 2.1 μmol/kg. The results of the DIC measurements for our study are shown in Table 1.

2.3. Analyses of calcites

2.3.1. Sample preparation

We used X-ray diffraction analyses to confirm that the precipitated phase is calcite. The largest calcite crystals were mounted in epoxy (EpoxiCure, BUEHLER) such that the pyramid base was exposed for SIMS analysis. Backscattered electron images demonstrated homogeneous intensity distribution within each individual crystal (Fig. S-2). The mounts were polished with 800 and 1200 grit SiC paper until the sample became flat, followed by polishing with diamond suspension of 3 μm in size. In order to reduce crystal relief development, down to a sub-micron level, the finest polishing with 1 μm alumina was conducted on the soft polish cloth for ~30 s. The sub-micron difference in the relief from the center to the edge of the crystals was determined by an interference microscope (PHASE SHIFT MicroXAM Surface Mapping Microscope Crystal) (see Gabitov et al., 2012 for details). No topography effect on Sr/Ca and Mg/Ca was found in the edge and the center of standard material. Samples were repolished in between two analytical sessions designated for Sr/Ca and Mg/Ca. Sr/Ca and Mg/Ca in calcite samples were determined using NBS-19 limestone, LAS-20 calcite, and UCI calcite reference materials. UCI is the most homogeneous standard where 1 s.e. (the standard deviation of multiple spots divided by the square root of the number of spots) is below 1% for both ratios. The Mg/Ca and Sr/Ca in all carbonate standards were determined using MC–ICP-MS and equal to 17.72 and 0.1912 mmol/mol (NBS-19); 45.01 ± 1.54 and 0.501 ± 0.030 mmol/mol (LAS-20); 3.446 ± 0.017 and 0.2043 ± 0.0004 mmol/mol (UCI) respectively (Gabitov et al., 2013).

Calcite crystals were analyzed by a CAMECA ims 1270 ion microprobe at UCLA. Quantitative Sr/Ca and qualitative REE/Ca were measured during analytical sessions 1 and 3. Subsequently, slow growing calcites were polished to remove about 10 μm of calcite and analyzed for Mg/Ca (analytical session 2). The combined analyses of Mg, Sr, and REE require switching of the magnet through the large mass range

Table 1
Composition of the sampled fluids in DC-1 experiment.

Sub-sample	t days	Mg/Ca mmol/mol	Sr/Ca mmol/mol	Ca μmol/kg	pH	DIC μmol/kg	CO_3^{2-} μmol/kg	Ω
Slow growth run DC-1 (24.6 ± 0.2 °C)								
Initial	−43	77.8	8.62	8166.6	5.5	Low	Low	Low
Nd-spike	36	116.9	12.43	3929.8	8.06	2410	170.2	1.95
Tb-spike	86	127.9	13.76	3590.5	8.15	2685	229.9	2.40
Final	150	189.1	20.23	2375.4	8.17	2775	247.8	1.71

Initial solution is the same for all experiments.
t is the time of crystallization from the addition of Sm spike. Initial time was estimated as 43 days prior to Sm addition by visual monitoring of the experimental flask with the naked eye every 1–2 days.
Sm, Nd, and Tb correspond to the fluid sub-sample collected just before addition of REE. The instrumental error of pH is 0.02.
mmol/mol corresponds to millimole of Mg or Sr divided by mole of Ca in solution.
pH of the fluid at the onset of crystallization was estimated to be 7.96 ± 0.06, which is the average of pH values at t = −8 and t = 0 days.
Sr/Ca and Mg/Ca in fluids from fast growth rate experiments are presented in Tables 2 and 3.
CO_3^{2-} and Ω calculations were performed using an excel implementation of CO2SYS (Lewis and Wallace, 1998), modified to use measured calcium concentrations. The constants of Millero (1995) were used for the carbonate and sulfate system. Salinity (S) of 29.4‰ was estimated by the amount of salts added into the initial fluid. The solubility product of calcite (K_{sp}^*) was calculated using the expression developed by Mucci (1983), yielding pK_{sp}^* of 6.46. CO_3^{2-} and Ω values presented in this work should be considered instead of those published by Gabitov et al. (2012) for the same experiment.
ICP-OES instrumental 1σ = 0.2%, dilution error 2%.

which caused an increase of the uncertainty by 0.5–1%; therefore, two types of analytical sessions with different mass ranges were performed. Composition of fast grown calcite was determined in the adjacent SIMS profiles during sessions 2 and 3. Mg/Ca and Sr/Ca were monitored in carbonate standard materials during each day of analyses.

2.3.2. Sr and REE analyses by SIMS

Individual crystals were analyzed with a 3–18 nA $^{16}O^-$ primary beam at 20–30 μm lateral dimension on the sample surface. Positive secondary ions corresponding to mass/charge stations of 41.7 (background), ^{42}Ca, 87.5 (background), ^{88}Sr, ^{139}La, ^{141}Pr, ^{143}Nd, ^{149}Sm, and ^{159}Tb were measured during analytical sessions 1 and 3. Count rates were varied from $1.3 \cdot 10^5$ to $1.8 \cdot 10^5$ counts per second (cps) for ^{42}Ca, from $5.8 \cdot 10^3$ to $1.1 \cdot 10^4$ cps for ^{88}Sr, and from 0 to 41 cps for REE. To reduce molecular interferences, Ca and REE were analyzed with a sample voltage offset of −60 V, and Sr was measured with the offset of −80 V using the energy bandwidth of 50 V (total voltage was 10 keV). Intensities were measured by peak switching with waiting times of 1–3 s and counting times of 1, 3, and 10 s for ^{42}Ca, ^{88}Sr, and REE, respectively. It was shown that energy filtering reduces molecular interferences during measurements of ^{42}Ca and ^{88}Sr from carbonate materials (Herzog et al., 1973; Shimizu et al., 1978; Allison, 1996; Hart and Cohen, 1996; Denniston et al., 1997; Gaetani and Cohen, 2006; Gabitov et al., 2013). The described analytical method allows for the reduction of potential molecular interferences for ^{42}Ca and ^{88}Sr to <0.3%. Our tests confirmed the findings of the aforementioned studies. REE measurements were only applied to determine the deviation of REE from the background in REE-spiked zones, i.e. the quantification of REE/Ca was not a goal of this work.

2.3.3. Mg analyses by SIMS

Individual crystals were analyzed with a 7 nA $^{16}O^-$ primary beam at 10 keV voltage and 20–30 μm lateral dimension on the sample surface. Positive secondary ions corresponding to mass/charge stations of ^{24}Mg and ^{42}Ca were measured during analytical session 2. Count rates were varied from $4.9 \cdot 10^5$ to $6.9 \cdot 10^5$ counts per second (cps) for ^{42}Ca and from $2.4 \cdot 10^4$ to $1.3 \cdot 10^5$ cps for ^{24}Mg. Analyses were performed at mass resolving power (MRP) of 3000, which is sufficient to resolve potential molecular interferences such as $^{12}C_2$, $^{23}Na^1H$, $^{26}Mg^{16}O$, and $^{40}Ca^1H_2$ (Gabitov et al., 2011; etc.).

3. Results

3.1. Composition of the fluids

For the slow growth experiment (DC-1), the concentrations and values of Mg^{2+}, Ca^{2+}, Sr^{2+}, pH, DIC, CO_3^{2-}, and saturation state with respect to calcite (Ω) in the fluid are presented in Table 1. Calculations of CO_3^{2-} were performed using an excel implementation of CO2SYS (Lewis and Wallace, 1998). The value of Ω was determined as $Ca^{2+} \cdot CO_3^{2-}/K^*_{sp}$, where K^*_{sp} is the stoichiometric solubility constant of calcite in seawater determined from the relationship developed by Mucci (1983), yielding pK^*_{sp} of 6.46 at T = 24.6 °C and salinity of 29.4‰. Because of the continuous precipitation of calcite, Ca concentrations decreased, but CO_3^{2-} increased in the solution for the duration of the slow growth experiment, hence affecting the calcite saturation state. The change of Sr/Ca and Mg/Ca with time (t, days) can be fitted with the polynomial functions for slow growth experiment:

$$Sr/Ca(mmol/mol) = 1.9 \cdot 10^{-4} \cdot t^2 + 0.037 \cdot t + 10, R^2 = 0.98 \quad (1)$$

$$Mg/Ca(mmol/mol) = 1.7 \cdot 10^{-3} \cdot t^2 + 0.37 \cdot t + 93, R^2 = 0.97. \quad (2)$$

Fluid Me/Ca increased by more than the a factor of two over the duration of the slow growth experiment. Almost the entire size of the crystals precipitated before adding the Sm spike to the fast growth experiments DC-3 and DSC-4 (see next section for details). Therefore, the average fluid values of $(Me/Ca)_{initial}$ and $(Me/Ca)_{Sm}$ were used to calculate K^{Sr} and K^{Mg} for calcites in the fast growth runs and fluid data from these experiments are not fitted.

3.2. Determination of growth rate

SIMS analyses of the slow grown calcites yielded the REE pattern, which corresponds to the introduction of REE elements into the growth medium. REE contours of the largest crystal are presented in Fig. 2. Here, ion beam burn marks are labeled by the REE elements, which were detected at the nearest spot to the crystal center. The appearance of REE corresponds to the sequence of its addition into fluid, i.e. starting with Sm and ending with Tb, and Pr. These REE-bearing spots are connected with each other, forming the REE-bearing contours representing the record of the crystal growth. The growth rates were determined as the width of each zone (Δx) in each profile divided by the time between REE spikes (Δt) (here Δt values are not equal to each other). Growth rates in the crystal interiors are higher than at the edges, i.e. V decreased from 0.169 to $1.4 \cdot 10^{-3}$ nm/s in the Sm–La and Tb–Pr zones respectively. This V trend is not a function of the cubed root of the volume of precipitated single crystal as estimated in Gabitov and Watson (2006), likely because of a decrease in the Ca/CO_3 ratio in the fluid with time and continuous nucleation of calcite in our experiments. The influence of the fluid Ca/CO_3 ratio on calcite step velocities (not necessarily the same as V) is described in Stack and Grantham (2010), which are higher than the growth rates for the range of Ca/CO_3 determined in our study.

In the fast growth experiments most calcites precipitated before addition of Sm (the first REE spike). In all cases, all REE spikes were detected in the individual spots at the edge of the crystals only. Here, the more intense CO_2 flux yielded higher saturation states that promoted rapid crystallization. The growth rates were estimated as no lower than 1.8 nm/s, because crystals grew overnight up to a few hundreds of microns in size.

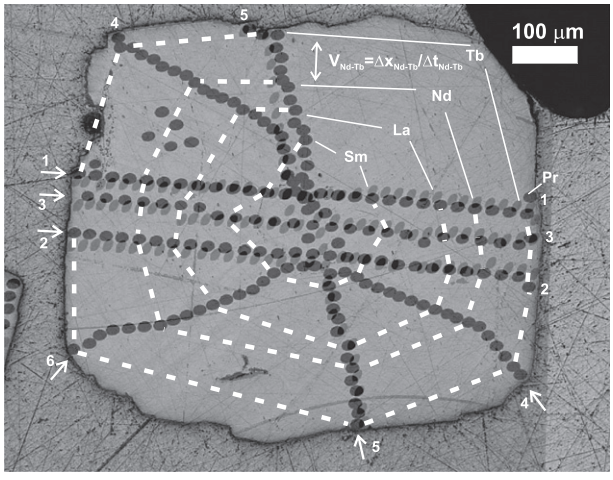

Fig. 2. A photomicrograph of a slow grown calcite crystal (DC-1, crystal-1). Images of the crystal after Sr/Ca and REE SIMS analysis and after Mg/Ca SIMS analysis have been superimposed. Circular and oval spots correspond to the ion beam burn marks from Sr/Ca (and REE) and Mg/Ca analyses respectively. Direction and number of profiles are shown with arrows and numbers next to it and at the other side of the crystal. Here, Sr and REE were determined in six ion microprobe profiles from one crystal edge to another (except profile 6—edge to center). Mg was analyzed in two perpendicular traverses across the crystal that correspond to REE profiles 3 and 5. Arrows show the direction of SIMS spot analyses in each profile. REE labels are appearing in the sequence of its detection by SIMS, which correspond to the sequence of REE addition into fluid during calcite growth. The dashed lines connect the spots with the particular REE element forming the contours of REE distribution within the crystal.

3.3. Composition of the calcite

An example of $^{149}Sm/^{42}Ca$, $^{139}La/^{42}Ca$, $^{143}Nd/^{42}Ca$ and Sr/Ca data from the slow growth experiment and Mg/Ca data through the similar space but 10 μm deeper is shown in Fig. 3A. Tb and Pr are not shown here because they appeared only at the edges of the crystals. SIMS count rates for Ca and REE are presented in the supplemental materials (Table S-1) of Gabitov et al. (2012). Sr/Ca and Mg/Ca show the reverse trends from the Sm spiked spots toward the edges, which is consistent with the studies of Gabitov (2005, 2010), Gabitov and Watson (2006), and Saulnier et al. (2012). These ratios are relatively stable at the earlier crystallization zone (La–Nd). Sr/Ca becomes more variable in the Sm–La zone and forms U-shape pattern with the minimum value around the center of the crystal where nucleation occurred. Mg/Ca is low at the center of the crystal relative to its edges. Sr/Ca and Mg/Ca evolution in the fluid is presented in Fig. 3B, where experimental data are fitted using Eqs. (1) and (2).

Sr/Ca and Mg/Ca in the fast grown calcites (runs DC-3 and DSC-4) increased from the crystal center to its edges, as was observed for Sr/Ca and Mg/Ca in the cores of crystals from the slow growth run (crystal zone before addition of Sm spike). This observation suggests that high growth rate caused 100% entrapment of the near-surface region of calcite crystal by its lattice (see Appendix 1, Fig. S-3, and description of the growth entrapment model later in the text). The increase of Me/Ca from the center to the edge in the fast grown crystals likely corresponds to an increase of Me/Ca in the fluid over time.

3.4. Partition coefficients

Partition coefficients (K^{Me}) were calculated as $K^{Me} = [Me/Ca(t)_{calcite}]/[Me/Ca(t)_{fluid}]$ for the calcites from the slow growth run. Here, $Me/Ca(t)_{calcite}$ is the averaged SIMS data from a particular REE-spiked zone of the calcite. The uncertainty in $Me/Ca(t)_{calcite}$ is the standard error (1 s.e.) of these data. $Me/Ca(t)_{fluid}$ was determined using the empirical Eqs. (1) and (2).

The data for each crystal were averaged in the runs with fast grown calcites due to the lack of REE in the crystal interior. K^{Me} was determined from the average $(Me/Ca)_{calcite}$ and the average of $(Me/Ca)_{fluid}$ between the initial fluid and when the Sm spike was added. The large error bars in K^{Me} are due to the variability of Me/Ca between multiple spots in a particular REE-spiked zone of the calcite; SIMS analytical uncertainty (1 s.e.) was less than 1% (Tables 2 and 3).

3.4.1. Strontium

In the slow growth run, K^{Sr} was independent on growth rate at V below 0.02 nm/s and increased by a factor of two with increasing of V from 0.02 to 0.2 nm/s (Fig. 4). Our data are consistent with other K^{Sr}–V studies as shown in Fig. 5. Calcite growth rates were determined directly in the current study whereas in Gabitov and Watson (2006) crystal V-values were estimated by assuming a constant flux of CO_3^{2-}. For better comparison, we converted the bulk precipitation rates from other studies (mol per area per time) into nm/s using the molar volume of calcite (36.93 cm^3/mol). This conversion should be treated with caution because precipitation of a single crystal was assumed for those studies. The three datasets suggest that K^{Sr} approaches the equilibrium value at V < 0.01 nm/s (Lorens, 1981; Tesoriero and Pankow, 1996, and this study). However, the "equilibrium" value of K^{Sr} of Tesoriero and Pankow (1996) is lower than ours and that of Lorens (1981) by a factor of two. In contrast, the data of Tang et al. (2008) are higher than ours by more than a factor of two. This discrepancy between different data sets cannot be explained by different Ca/CO_3^{2-} in the fluid, because Ca/CO_3^{2-} from our work is lower than those from studies of Lorens (1981),

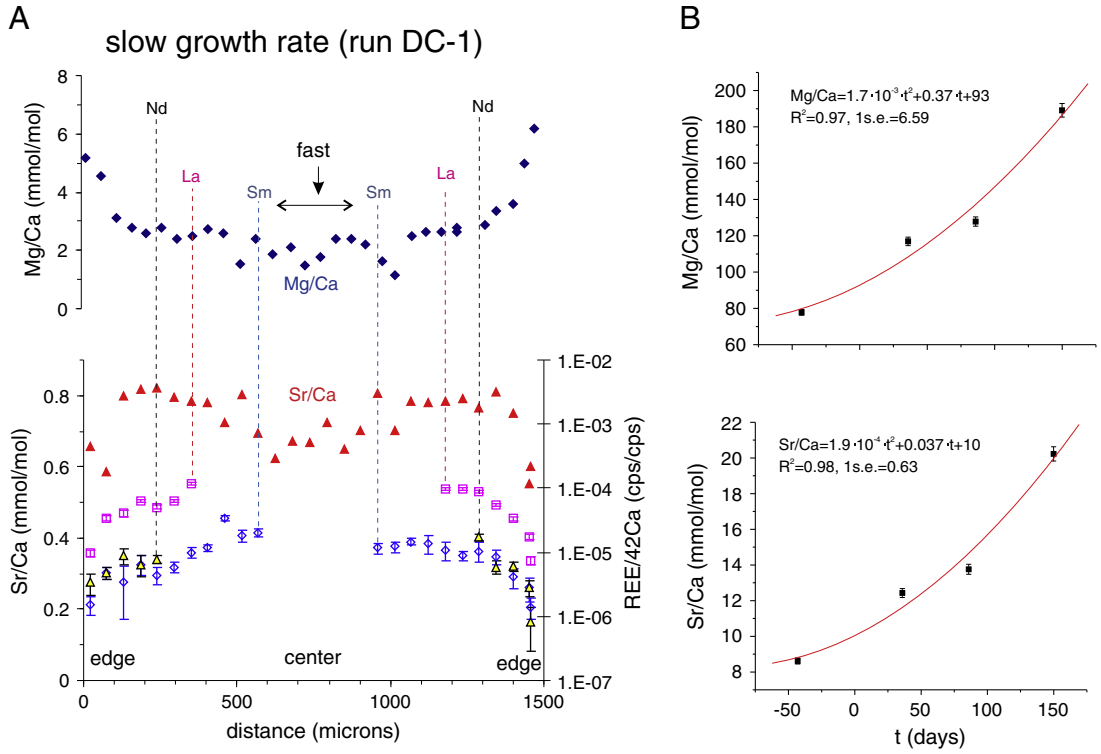

Fig. 3. An example of Sr/Ca and Mg/Ca evolution in calcite and fluid. Here, Sr/Ca (red solid triangles) and REE/^{42}Ca (blue empty diamonds, magenta empty rectangle, yellow solid triangle) are combined with Mg/Ca data (blue solid diamonds). REE/^{42}Ca is shown at the crystal zones illustrating the spike signal. A) Sr/Ca and Mg/Ca profiles across REE-spiked calcite crystals grown at slow rate. Sm, La, and Nd labeled vertical dashed lines are showing the nearest spots to the crystal center where the particular spike was detected. B) Sr/Ca and Mg/Ca in fluid of the slow growth run rates. Errors for all ratios are the s.e. at 1σ level. Error bars for Sr/Ca and Mg/Ca are smaller than the size of the symbols.

Table 2
Partitioning data of Sr.

REE	t (d)	V (nm/s)	V error	Sr/Ca calcite mmol/mol	s.e.	Sr/Ca[a] fluid mmol/mol	s.e.	K^{Sr}	s.e.
Slow growth run DC-1, Crystal 1, profile 1									
Nd–Tb	36–86	0.042	0.002	0.733	0.027	13.1		0.0560	0.0034
La–Nd	24–36	0.117	0.005	0.782	0.023	11.3		0.0693	0.0044
Sm–La	0–24	0.116	0.007	0.729	0.030	10.5		0.0694	0.0051
Sm–La	0–24	0.090	0.007	0.749	0.010	10.5		0.0713	0.0044
La–Nd	24–36	0.117	0.005	0.816	0.022	11.3		0.0722	0.0045
Nd–Tb	36–86	0.036	0.002	0.718	0.077	13.1		0.0548	0.0064
Slow growth run DC-1, Crystal 1, profile 2									
Nd–Tb	36–86	0.050	0.002	0.754	0.048	13.1		0.0576	0.0046
La–Nd	24–36	0.108	0.005	0.837	0.008	11.3		0.0741	0.0042
Sm–La	0–24	0.133	0.007	0.744	0.028	10.5		0.0709	0.0050
Sm–La	0–24	0.134	0.007	0.783	0.032	10.5		0.0746	0.0054
La–Nd	24–36	0.108	0.005	0.820	0.012	11.3		0.0726	0.0042
Nd–Tb	36–86	0.032	0.002	0.642	0.069	13.1		0.0490	0.0058
Slow growth run DC-1, Crystal 1, profile 3									
Nd–Tb	36–86	0.051	0.003	0.737	0.044	13.1		0.0563	0.0043
La–Nd	24–36	0.108	0.006	0.801	0.011	11.3		0.0709	0.0041
Sm–La	0–24	0.106	0.010	0.757	0.020	10.5		0.0721	0.0047
Sm–La	0–24	0.106	0.010	0.771	0.018	10.5		0.0734	0.0047
La–Nd	24–36	0.108	0.006	0.780	0.008	11.3		0.0690	0.0039
Nd–Tb	36–86	0.038	0.003	0.720	0.051	13.1		0.0550	0.0047
Tb–Pr	86–129	$1.4 \cdot 10^{-3}$		0.576	0.024	16.3		0.0353	0.0020
Slow growth run DC-1, Crystal 1, profile 4									
Tb–Pr	86–129	0.011	0.001	0.578	0.014	16.3		0.0355	0.0016
Nd–Tb	36–86	0.047	0.002	0.666	0.033	13.1		0.0508	0.0035
La–Nd	24–36	0.112	0.005	0.724	0.016	11.3		0.0641	0.0038
Sm–La	0–24	0.132	0.007	0.777	0.026	10.5		0.0740	0.0051
Sm–La	0–24	0.109	0.007	0.672	0.014	10.5		0.0640	0.0041
La–Nd	24–36	0.173	0.005	0.728	0.009	11.3		0.0644	0.0037
Nd–Tb	36–86	0.063	0.002	0.686	0.021	13.1		0.0524	0.0030
Tb–Pr	86–129	0.010	0.001	0.580	0.013	16.3		0.0356	0.0016
Slow growth run DC-1, Crystal 1, profile 5									
Nd–Tb	36–86	0.044	0.002	0.654	0.026	13.1		0.0499	0.0031
La–Nd	24–36	0.074	0.005	0.707	0.013	11.3		0.0626	0.0037
Sm–La	0–24	0.101	0.007	0.660	0.016	10.5		0.0629	0.0041
Sm–La	0–24	0.071	0.007	0.668	0.011	10.5		0.0636	0.0040
La–Nd	24–36	0.103	0.005	0.730	0.035	11.3		0.0646	0.0048
Nd–Tb	36–86	0.036	0.002	0.689	0.049	13.1		0.0526	0.0045
Slow growth run DC-1, Crystal 1, profile 6									
Nd–Tb	36–86	0.069	0.002	0.844	0.043	13.1		0.0644	0.0045
La–Nd	24–36	0.175	0.005	0.745	0.017	11.3		0.0659	0.0040
Sm–La	0–24	0.106	0.007	0.729	0.044	10.5		0.0694	0.0059
Slow growth run DC-1, Crystal 4, profile 1									
Nd–Tb	36–86	0.042	0.002	0.591	0.018	13.1		0.0451	0.0026
La–Nd	24–36	0.088	0.005	0.683	0.042	11.3		0.0604	0.0050
La–Nd	24–36	0.142	0.005	0.697	0.004	11.3		0.0617	0.0035
Nd–Tb	36–86	0.041	0.002	0.617	0.031	13.1		0.0471	0.0033
Slow growth run DC–1, Crystal 4, profile 2									
Nd–Tb	36–86	0.051	0.002	0.728	0.066	13.1		0.0556	0.0057
La–Nd	24–36	0.109	0.005	0.722	0.019	11.3		0.0639	0.0039
La–Nd	24–36	0.109	0.005	0.711	0.005	11.3		0.0629	0.0035
Nd–Tb	36–86	0.052	0.002	0.673	0.029	13.1		0.0514	0.0033
Slow growth run DC-1, Crystal 5, profile 1									
Nd–Tb	36–86	0.036	0.005	0.654	0.015	13.1		0.0499	0.0027
La–Nd	24–36	0.125	0.007	0.722	0.028	11.3		0.0639	0.0043
La–Nd	24–36	0.104	0.007	0.702	0.008	11.3		0.0621	0.0035
Nd–Tb	36–86	0.050	0.005	0.674	0.027	13.1		0.0515	0.0032
Tb–Pr	86–129	0.021	0.002	0.571	0.000	16.3		0.0350	0.0014
Slow growth run DC-1, Crystal 5, profile 2									
Tb–Pr	86–129	0.008	0.001	0.587	0.001	16.3		0.0360	0.0014
Nd–Tb	36–86	0.077	0.002	0.820	0.040	13.1		0.0626	0.0043
La–Nd	24–36	0.138	0.005	0.789	0.050	11.3		0.0698	0.0059
La–Nd	24–36	0.163	0.005	0.874	0.028	11.3		0.0773	0.0050
Nd–Tb	36–86	0.052	0.002	0.753	0.061	13.1		0.0575	0.0054

(continued on next page)

Table 2 (*continued*)

REE	t (d)	V (nm/s)	V error	Sr/Ca calcite mmol/mol	s.e.	Sr/Ca[a] fluid mmol/mol	s.e.	K^{Sr}	s.e.
Tb–Pr	86–129	0.014	0.001	0.547	0.012	16.3		0.0336	0.0015
Slow growth run DC-1, Crystal 6, profile 1									
Nd–Tb	36–86	0.062	0.002	0.751	0.033	13.1		0.0573	0.0037
La–Nd	24–36	0.175	0.005	0.803	0.006	11.3		0.0711	0.0040
La–Nd	24–36	0.179	0.005	0.915	0.017	11.3		0.0810	0.0048
Nd–Tb	36–86	0.063	0.002	0.756	0.042	13.1		0.0577	0.0042
Tb–Pr	86–129	0.013	0.001	0.645	0.007	16.3		0.0396	0.0016
Slow growth run DC-1, Crystal 6, profile 2									
La–Nd	24–36	0.164	0.002	0.794	0.006	11.3		0.0703	0.0040
La–Nd	24–36	0.153	0.005	0.755	0.025	11.3		0.0668	0.0043
Nd–Tb	36–86	0.061	0.005	0.766	0.028	13.1		0.0585	0.0035
Slow growth run DC-1, Crystal 6, profile 3									
Nd–Tb	36–86	0.053	0.002	0.685	0.023	13.1		0.0523	0.0031
La–Nd	24–36	0.136	0.005	0.807	0.035	11.3		0.0714	0.0050
La–Nd	24–36	0.157	0.005	0.740	0.014	11.3		0.0655	0.0039
Slow growth run DC-1, Bulk-2, Crystal-2									
Tb–Pr	86–129	0.0133	0.001	0.552	0.006	16.3		0.0339	0.0014
Nd–Tb	36–86	0.0404	0.002	0.655	0.023	13.1		0.0500	0.0030
Nd–Tb	36–86	0.0639	0.002	0.717	0.023	13.1		0.0547	0.0032
Tb–Pr	86–129	0.0036	0.001	0.659	0.011	16.3		0.0404	0.0017
Fast growth run DC-3, Cr1[b]									
Sm	0	≥1.8	n/a	3.53	0.21	22.5	0.6	0.157	0.044
Corrected to temperature of DC-1 (24.6 °C)								0.151	
Fast growth run DC-3, Cr2[b]									
Sm	0	≥2		3.80	0.27	22.5	0.6	0.169	0.048
Corrected to temperature of DC-1 (24.6 °C)								0.163	
Fast growth run DSC-4, Cr1[b]									
Sm	0	≥4.1	n/a	4.53	0.24	16.8	0.4	0.270	0.081
Corrected to temperature of DC-1 (24.6 °C)								0.254	
FAST growth run DSC-4, Cr2[b]									
Sm	0	≥3.9	n/a	3.38	0.22	16.8	0.4	0.201	0.061
Corrected to temperature of DC-1 (24.6 °C)								0.189	

Sr/Ca in calcite is the average of a few spot analyses in particular REE spiked zone; s.e. (1σ) is the standard deviation of multiple spots divided by the square root of the number of spots (n) in each REE spiked zone. n varies from 3 to 6 in all REE-spiked zones except Tb–Pr zone, where n = 1. Directly measured Sr/Ca concentrations are presented in Table 1.
In fast precipitation runs most of the growth occurred before the addition of 1st spike (Sm) therefore average Mg/Ca and Sr/Ca with initial fluid is considered in the runs DC-3 and DSC-4. pH during fast calcite precipitation should exceed the values recorded at the time of addition of Sm spike.
Data collected from the calcite REE-free core are not included here(see Appendix 1). Error for growth rate is estimated from the size of the ion beam and the time of the growth of particular area of calcite crystal.

[a] Fitting error (s.e. = 0.63) for Sr/Ca in fluid is based on four samples collected from slow precipitation experiment DC-1 (Eq. (1)).

[b] Errors for Sr/Ca in the fluid are 1 s.e. (1σ) of multiple sub-samples collected during calcite growth in fast precipitation experiments (DC-3 and DSC-4).

Tesoriero and Pankow (1996), and Tang et al. (2008). Different methods of growth rate determination are most likely the main cause for the variations in K^{Sr}-rate relationships from one study to the other. Our highest K^{Sr} (fast growth runs: DC-3 and DSC-4) overlaps with those from Gabitov and Watson (2006) at V > 2 nm/s, when K^{Sr} becomes scattered but significantly less dependent of the growth rate. From the fast growth runs, K^{Sr} was corrected to the few degrees of temperature difference with highest K^{Sr} from slow growth run (DC-1) using calibrations of Gabitov and Watson (2006), which yields a decrease of K^{Sr} by 3.5% (DC-3) and 5.9% (DSC-4).

3.4.2. Magnesium

In contrast to K^{Sr}, K^{Mg} decreased with increasing growth rate (Fig. 6). K^{Mg} decreased by ~33 ± 16% when V increased from $1.4 \cdot 10^{-3}$ to 0.06 nm/s (slow growth run). K^{Mg} from the fast growth runs was corrected to the temperature difference with lowest K^{Mg} from DC-1 using calibrations of Mucci (1987), which yields the increase of corrected K^{Mg} by 6.7% (DC-3) and 12.2% (DSC-4). Our data regarding slow calcite growth is consistent with from the findings of Mucci and Morse (1983) and Huang and Fairchild (2001). It is important to note that the fluid Mg/Ca are different by up to a factor of fourteen between experiments presented in Fig. 6, because Mucci and Morse (1983) reported high sensitivity of K^{Mg} to fluid Mg/Ca. In our experiments, calcite grew in solutions where Mg/Ca varied from 77.8 to 281 mmol/mol, which is lower than those in Mucci and Morse (1983) (Mg/Ca = 10^3 mmol/mol) and higher than the fluid Mg/Ca in Huang and Fairchild (2001) (Mg/Ca = 25 mmol/mol). The effect of fluid Mg/Ca on K^{Mg} should be examined at lower values of Mg/Ca relative to those reported by previous studies (Mucci and Morse, 1983; Mavromatis et al., 2013).

3.5. Simulation using the growth entrapment model (GEM)

The model of Watson and co-workers was used to test our experimental data (Watson and Liang, 1995; Watson, 1996, 2004). The model assumes a presence of a few angstroms thick of the near-surface region of the crystal where solid state diffusion (D_s) is much faster than diffusion in the crystal lattice (D_l) ($D_s \approx 10^{16} D_l$). This assumption is reasonable due to the existence of the calcite surface layer, which is structurally different from the calcite lattice (Fenter et al., 2000). This large diffusivity difference is consistent with the results of cadmium uptake in calcite from the work of Stipp et al. (1992). According to the results applying the GEM, the near-surface region is enriched or depleted in Me relative to the crystal lattice and is characterized by a parameter F, where F is the ratio of Me in the near surface region of the crystal to Me in the lattice at equilibrium conditions. During very fast growth this distinct surface composition is being fully captured by new-formed lattice representing a 100% entrapment, i.e. K^{Me}(lattice) = K^{Me}(surface).

Table 3
Partitioning data of Mg.

REE	t (d)	V (nm/s)	V error	Mg/Ca calcite mmol/mol	s.e.	Mg/Ca fluid mmol/mol	s.e.	K^{Mg}	s.e.
Slow growth run DC-1, Crystal 1, profile 3									
Nd–Tb	36–86	0.051	0.003	3.50	0.45	123		0.0285	0.0040
La–Nd	24–36	0.108	0.006	2.59	0.09	106		0.0245	0.0018
Sm–La	0–24	0.106	0.010	2.31	0.27	97.8		0.0236	0.0032
Sm–La	0–24	0.106	0.010	2.34	0.30	97.8		0.0239	0.0035
La–Nd	24–36	0.108	0.006	2.73	0.05	106		0.0258	0.0017
Nd–Tb	36–86	0.038	0.003	3.70	0.45	123		0.0301	0.0040
Tb–Pr	86–129	$1.4 \cdot 10^{-3}$	n/a	5.57	0.61	153		0.0363	0.0043
Slow growth run DC-1, Crystal 1, profile 5									
Nd–Tb	36–86	0.044	0.002	3.65	0.51	123		0.0297	0.0044
La–Nd	24–36	0.074	0.005	2.40	0.04	106		0.0227	0.0015
Sm–La	0–24	0.101	0.007	2.32	0.07	97.8		0.0237	0.0018
Sm–La	0–24	0.071	0.007	2.30	0.12	97.8		0.0235	0.0020
La–Nd	24–36	0.103	0.005	2.54	0.06	106		0.0240	0.0016
Nd–Tb	36–86	0.036	0.002	3.02	0.29	123		0.0246	0.0027
Slow growth run DC-1, Crystal 5, profile 1									
Nd–Tb	36–86	0.036	0.005	2.77	0.15	123		0.0225	0.0017
La–Nd	36	0.125	0.007	2.20	0.20	106		0.0208	0.0023
La–Nd	36	0.104	0.007	2.26	0.15	106		0.0213	0.0019
Nd–Tb	36–86	0.050	0.005	2.91	0.36	123		0.0237	0.0032
Slow growth run DC-1, Crystal 6, profile 1									
Nd–Tb	36–86	0.062	0.002	3.31	0.29	123		0.0269	0.0028
La–Nd	36	0.175	0.005	2.47	0.02	106		0.0233	0.0015
La–Nd	36	0.179	0.005	2.53	0.05	106		0.0239	0.0016
Nd–Tb	36–86	0.063	0.002	2.56	0.20	123		0.0208	0.0020
Tb–Pr	86–129	0.013	0.001	4.31	0.78	153		0.0282	0.0052
Fast growth run DC-3, Cr1[a]									
Prior Sm	0	≥2	n/a	3.45	0.82	281	7	0.012	0.005
Corrected to temperature of DC-1 (24.6 °C)	0.013								
Fast growth run DSC-4, Cr1									
Prior Sm	0	≥4	n/a	1.86	0.21	211	5	0.009	0.003
Corrected to temperature of DC-1 (24.6 °C)[a]	0.010								
Fast growth run DSC-4, Cr2									
Prior Sm	0	≥4	n/a	2.34	0.21	211	5	0.011	0.004
Corrected to temperature of DC-1 (24.6 °C)[a]	0.012								

Mg/Ca in calcite is the average of a few spot analyses in particular REE spiked zone. Fitting error (s.e. = 6.59) for Mg/Ca in fluid is based on four samples collected from slow precipitation experiment DC-1 (Eq. (2)). Directly measured Mg/Ca concentrations are presented in Table 1.
Data collected from the calcite REE-free core are not included here (see Appendix 1). Error for growth rate is estimated from the size of the ion beam and the time of the growth of particular area of calcite crystal.
[a] Errors for Mg/Ca in the fluid are s.e. (1σ) of multiple sub-samples collected during calcite growth.

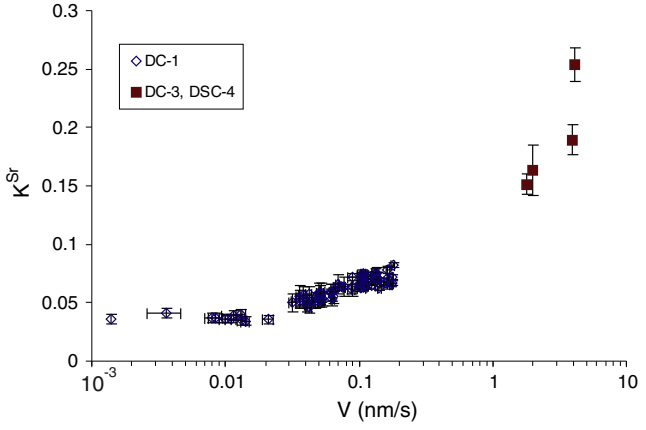

Fig. 4. Strontium partition coefficient versus calcite growth rate. The data collected in the calcite zones grown after Sm spike addition to the run DC-1 were used to calculate partition coefficients (diamonds). Error for growth rate is estimated from the size of the ion beam and the time of the growth of particular area of calcite crystal. Averaged Sr/Ca were used to calculate K^{Sr} in the fast precipitation experiments (DC-3 and DSC-4, rectangles).

Here, K^{Me}(surface) is an equilibrium partition coefficient of Me between the near surface enriched region and the fluid. As a result, disequilibrium partitioning of Me between lattice and near-surface region, and hence between lattice and fluid, occurs. During very slow growth, D_s is fast enough to equilibrate the near-surface region with new-formed lattice,

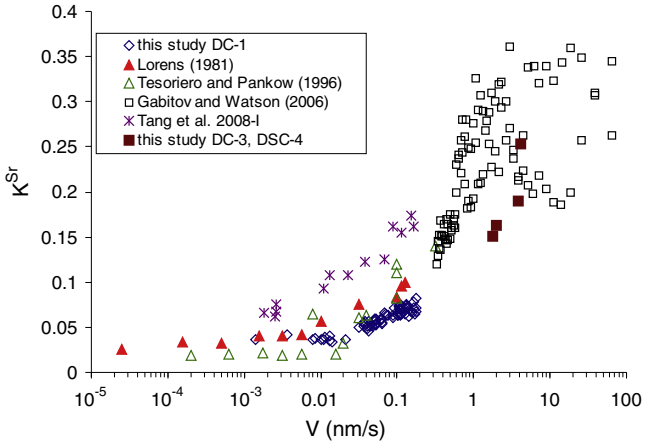

Fig. 5. Comparison of K^{Sr} from this study with literature data.

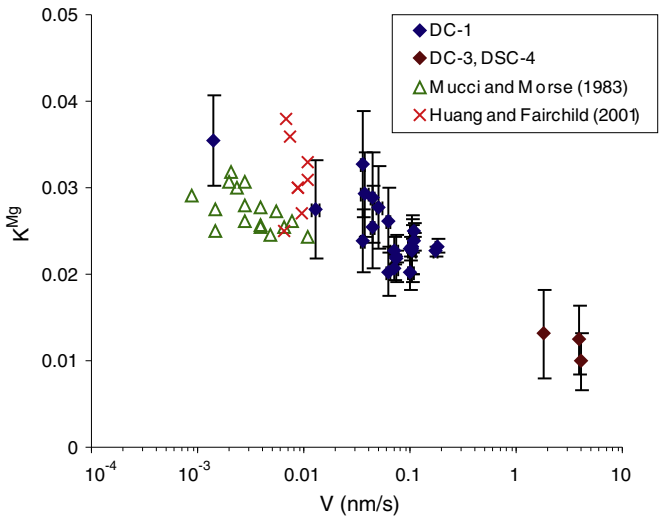

Fig. 6. Comparison of K^{Mg} from this study with literature data. Calculations of partition coefficients and growth rate uncertainties are described in the caption of Fig. 4.

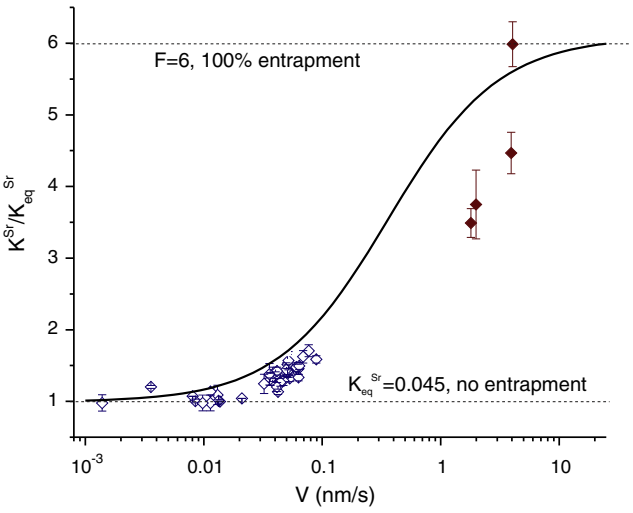

Fig. 7. Ratio of measured K^{Sr} to its assumed equilibrium value (K^{Sr}_{eq} is the smallest K^{Sr} from our data) versus calcite growth rate. Solid curve represents GEM derived data. Empty diamonds correspond to the experimental data from the run DC-1; solid diamonds are from the runs DC-3 and DSC-4. Upper dashed line shows the highest degree of entrapment when the lattice composition is approaching those of the surface. Lower dashed line corresponds to the equilibrium growth without growth entrapment.

representing an equilibrium partitioning, i.e. K^{Me}(lattice) = K^{Me}_{eq}(lattice). At intermediate growth rates, partial growth entrapment happens (Appendix 2). The GEM was successfully used to explain the experimental data of Sr, Mg, and $^{18}O/^{16}O$ versus V in calcite and aragonite (Stoll et al., 2002b; Gabitov et al., 2008; Tang et al., 2008; Holcomb et al., 2009; Gabitov et al., 2012; Saulnier et al., 2012; Gabitov, 2013).

Ab initio molecular dynamics simulations of Ti^{4+} in the near-surface region of α quartz confirmed the validity of GEM as well (Lanzillo et al., in press). It is quantitatively demonstrated that vacancy-formation energy of Ti^{4+} in the outermost monolayers of quartz is significantly smaller than in the crystal interior (bulk lattice). Lanzillo et al. provide evidence for the fast Ti diffusivity in the near surface region of quartz by showing that the activation energy for Ti diffusion decreases steeply toward the crystal surface in the 2–3 outermost monolayers.

3.5.1. Strontium

To compare modeling and experimental results the obtained partition coefficients were normalized to their equilibrium value (K^{Sr}_{eq}), which was considered to be 0.0451 (the minimal values in the slow growth run). The maximum observed K^{Sr} (K^{Sr}_{max}) of 0.254 ± 0.081 (fast growth run DSC-4) is consistent with average maximum K^{Sr} of 0.269 ± 0.014 from Gabitov and Watson (2006). Therefore, the value of F^{Sr} was considered to be equal to $K^{Sr}_{max}/K^{Sr}_{eq} = 6$. Fig. 7 shows K^{Sr}/K^{Sr}_{eq} versus V, where $D_s = 0.1$ nm²/s. Sr partitioning increases by more than a factor of five when V increases from 0.01 to 10 nm/s. GEM suggests that K^{Sr} is independent of V at very slow rates (V < 0.001 nm/s) and is not subject for strong V effect at very fast rates (V > 10 nm/s) calcite growth.

3.5.2. Magnesium

Our highest K^{Mg} obtained from the slowest zone of calcite was assumed to represent an equilibrium between calcite lattice and fluid (K^{Mg}_{eq} = 0.0363, DC-1). The equilibrium partition coefficient between calcite surface and fluid ($K^{Mg}_{surface}$) was assumed to be equal to the smallest K^{Mg} = 0.009 in our experiments (fast growth run DSC-4) (K^{Mg} < 0.01 was not observed in the literature). These parameters yield F^{Mg} of 0.3. Fig. 8 shows K^{Mg}/K^{Mg}_{eq} versus V, where $D_s = 0.1$ nm/s. GEM suggests that Mg partitioning decreased by a factor of three when V increased from 0.005 to 5 nm/s and becomes independent on growth rate at V < 0.001 nm/s and V > 10 nm/s.

4. Discussion

Our results show a reverse behavior of Sr and Mg with increasing calcite growth rates, i.e. K^{Sr} increases and K^{Mg} decreases with the advancing rate of the crystal surface growth. The data are consistent with GEM simulations, which imply fast diffusivity of Sr and Mg in the near-surface layer of calcite. According to the results from the GEM simulations, Sr is enriched and Mg is depleted in the near-surface layer of calcite relative to the bulk lattice. Also, the simulation results suggest that equilibrium partitioning of Sr and Mg occur at growth rates slower than 0.001 nm/s, i.e. when no growth entrapment occurs. The 100% entrapment happens at high growth rates of faster than 10 nm/s, where $K^{Sr} = F^{Sr} = 6$ and $K^{Mg} = F^{Mg} = 0.3$. Therefore, growth rate influence

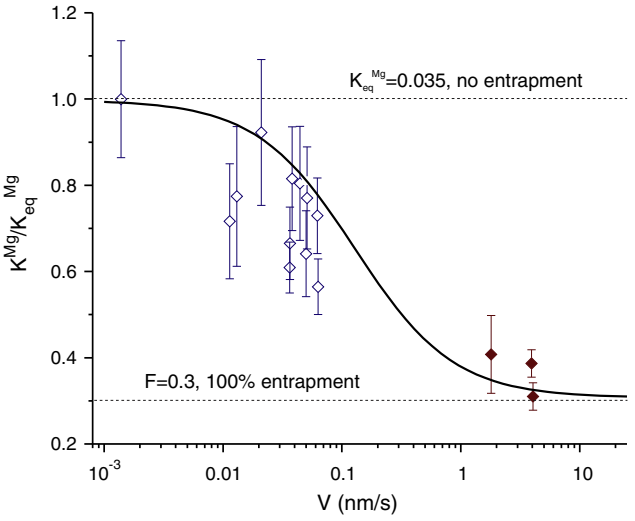

Fig. 8. Ratio of measured K^{Mg} to its equilibrium value (K^{Mg}_{eq} is assumed to be equal to the highest K^{Mg} from this study) versus calcite growth rate. Diamonds and fitting curve represent experimental and GEM derived data, respectively (see caption of Fig. 7). Upper dashed line corresponds to the equilibrium growth without growth entrapment. Lower dashed line shows the highest degree of entrapment when lattice composition approaching those of surface.

masks the temperature effect on K^{Sr} and K^{Mg} if compared to extremely slow or fast growth of calcite.

There is another potential explanation for decrease of K^{Mg} with increasing V because it is consistent with slow Mg dehydration relative to Ca. It was shown that $Mg^{2+}(H_2O)_6$ and $Ca^{2+}(H_2O)_6$ are the most stable species and $Mg^{2+}(H_2O)_6$ dissociates slower than $Ca^{2+}(H_2O)_6$ at temperatures below 60 °C (Pavlov et al., 1998; Rodriguez-Cruz et al., 1999a,b). Therefore, slow dissociation of $Mg^{2+}(H_2O)_6$ could contribute to decrease of Mg partitioning at high growth rate. It was shown that the rate of water molecules exchange for $Mg^{2+}(H_2O)_6$ is four orders of magnitude lower than for $Ca^{2+}(H_2O)_6$ (Lincoln and Merbach, 1995; Bleuzen et al., 1997; Schott et al., 2009). However, such input caused by slow Mg dehydration contradicts with positive dependence of K(Mg) on calcite precipitation rate (Mavromatis et al., 2013). Also, they reported decrease of K(Mg) with increasing of Mg/Ca in the fluid. There is no overlap (except one datum) of their Mg/Ca_{fluid} (220–1370 mmol/mol) with ours (98–280 mmol/mol). The opposite K(Mg)–V dependence between our study and Mavromatis et al. (2013) potentially could be explained by different Mg/Ca in the fluid, which may cause the change of Mg incorporation mechanism. The variable Mg structural state in calcite was determined by Finch and Allison (2007), who suggested that significant portion of Mg presents as nanodomains in calcite. However, this cannot explain stronger dependence of K(Mg) on Mg/Ca_{fluid} than on Mg_{fluid} from Mavromatis et al. (2013). Mucci and Morse (1983) observed negative effect of Mg/Ca_{fluid} on K^{Mg} as well. They reported exponential decrease of K^{Mg} with increasing fluid Mg/Ca when $Mg/Ca_{fluid} \leq 7.5$ mol/mol. Their inorganic data are consistent with the K^{Mg}–$Mg/Ca_{seawater}$ trend observed in benthic foraminifera (Segev and Erez, 2006; Raitzsch et al., 2010). However, if this effect would control Mg partitioning, then K^{Mg} would be lower at the edge of calcite crystals, which is opposite to our results. Our finding is consistent with the data of Katz (1973) who reported uniform K^{Mg} of 0.053 ± 0.0017 in fluid Mg/Ca from 1 to 4 mol/mol. Small pCO_2 variability ($5.7 \cdot 10^{-4}$–$6.5 \cdot 10^{-4}$ atm) unlikely affects our K^{Mg}, which is consistent with the results of Hartley and Mucci (1996), where pCO_2 varied from 10^{-5} to 0.32 atm.

Our data have an important implication for Mg/Ca in planktonic foraminifera. Despite the large difference of Mg/Ca in experimental fluid relative to $Mg/Ca_{seawater}$ the range of Mg/Ca in calcite crystal (1–7 mmol/mol; see Fig. 3A) is within the range observed in foraminifera shells (1–10 mmol/mol; Erez, 2003; Eggins et al., 2004; Anand and Elderfield, 2005; Sadekov et al., 2005; Kunioka et al., 2006). To explain this variation several hypotheses have been suggested that predominantly links foraminiferal biological activity with Mg incorporation into biominerals (see Bentov and Erez, 2006 for review). For example, Kunioka et al. (2006) proposed that Mg variability in foraminiferal calcite reflects the proportion of organic compounds embedded in the crystals or between them. Work of Eggins et al. (2004) suggested that variation in Mg/Ca values could be explained by changes in seawater pH in foraminiferal microenvironment driven by diurnal photosynthetic activity of symbiotic algae. However, our work shows that similar amplitude of Mg/Ca variation in biominerals can be explained by inorganic processes, whereas the low Mg/Ca in foraminifera with respect to seawater is probably caused by biological activity.

Estimations on how V affects K^{Me} in stalagmites and marine biogenic calcite were performed for the growth rates reported in the literature. The growth rate ranges are: 0.001–0.09 nm/s in stalagmites (Baker et al., 1998); 0.002–0.04 nm/s in coccolithophores (Stoll et al., 2002b), 0.08–0.3 nm/s in foraminifera (ter Kuile and Erez, 1984); and 0.1–3.3 nm/s in mollusks (Owen et al., 2002; Freitas et al., 2009). The reported increasing growth rates elevate K^{Sr} by 50% in coccolithophores and foraminifera, by 100% in stalagmites, and by more than 200% in mollusks. Growth rate values of naturally occurring calcites values reported above are approximate, because of the presence of pores, polycrystalline nature of biogenic calcite, and its episodic growth. It is reasonable to consider the growth band pattern in biogenic carbonates, which suggests that crystallization occurs episodically, i.e. there are temporal phases when $CaCO_3$ is formed and phases when no precipitation occurred (Erez, 2003). Therefore, extension rates of biogenic calcites based on the size change over time may be underestimated by up to the factor of two. This crystallization scenario is different from continuous growth of calcite in inorganic experiments, and therefore, should be considered when applying laboratory data to natural samples.

Acknowledgments

We would like to thank Bruce Watson for discussing our data in the prospect of diffusion-controlled crystal growth and for providing the GEM code. We gratefully acknowledge Axel Schmitt, Kevin McKeegan, and Mark Harrison for their help and support with the ion microprobe analyses. Experiments and SIMS analyses were supported by the U.S. NSF, EAR, Instrumentation and Facilities Program. We thank ICP-OES laboratory at the University of Edinburgh and Walter Geibert for support in fluid Me/Ca analyses. DIC analyses were covered by ETH grant no. 4 443869-AL-20600. We also thank the Institute for Imaging and Analytical Technologies and Mississippi State University for support in XRD analyses. We are grateful to Ellen Druffel, Neil Sturchio, and Kevin McKeegan for providing calcite standards. We thank Jeremy Weremeichik and Dinah Gabitov for their comments on the manuscript preparation. Finally we would like to thank Heather Stoll for her comments which help to improve the presentation of our work; Nicola Allison, Bruno Thien, two anonymous reviewers, and Editor-in-Chief Jeremy Fein for reviewing the previous version of the manuscript.

Appendix 1. Sr/Ca and Mg/Ca distribution within calcite crystals

Sr/Ca is depleted in the calcite rim in the slow growing crystals, indicating the domination of V over the reservoir effect (i.e., increase of fluid Sr/Ca with time) (Fig. 3A). However, Sr/Ca rapidly increases from the center of calcite to its edge in the fast growing crystals (Fig. S-1). Similar trends were observed in the ~500 μm rapidly grown cores in the crystals of the slow growth run (Fig. 3A). In addition, Sr/Ca in the calcites from the fast growth runs is higher than in those from the slow growth experiment by about a factor of three, despite the use of the same initial fluid for all runs. There are two possible scenarios that could explain this Sr/Ca controversy: 1) the increase of fluid Sr/Ca during crystallization; 2) the formation of a distinct fluid boundary layer adjacent to the calcite surface in the fast runs.

1) Sr/Ca increases toward the rim of calcite by the factor two or three, which is quantitatively consistent with the increase of fluid Sr/Ca from 8.6 to 22.5 and 16.8 mmol/mol during fast calcite growth. The ~10% rise of fluid Sr/Ca is consistent with calcite Sr/Ca increase from the crystal center to the zone where Sm (the 1st REE spike) showed up in the slow growth run.
2) The formation of a diffusive boundary layer between calcite surface and the fluid is possible in the fast growth runs ($V > 2$ nm/s). These core data were collected in the calcite zones with estimated growth rates ($V < 0.2$ nm/s), which are too slow to cause appearance of the boundary layer between calcite and fluid where ion diffusion is very fast ($D_{Me} \approx 10^9$ nm^2/s) (Smith et al., 1955; Li and Gregory, 1974; Watson and Müller, 2009).

We think that the first scenario better describes the Sr/Ca behavior in the fast growth crystals. When $V > 2$ nm/s, Sr/Ca in calcite reflects only the fluid Sr/Ca changes and K^{Sr} is constant within the fast grown calcite crystals, because of similarity between Mg/Ca profiles in the slow and fast growth experiments. The Mg/Ca data support the absence of the distinct fluid boundary layer at the surface of calcite. Mg/Ca ratios within a single calcite crystal have a similar pattern in all analyzed calcites: it sharply increases in the 100 μm thick rim relative to the calcite

interior. Therefore, Mg/Ca signature in calcite is being controlled by changing of reservoir fluid composition and crystal growth rate.

Appendix 2. Parameters for the growth entrapment model

The simulations were conducted with the new version of the GEM code (GEM2) running with QB64. The description of the model is presented by Watson (2004), where he considered that concentration of Me changes as a function of the distance from the surface of the crystal:

$$Me(x) = Me_{eq} \cdot F^{\exp(x/l)} \quad (A1.1)$$

where $Me(x)$ is the concentration of Me in the crystal at some distance x from the surface, Me_{eq} is the concentration reflecting partition equilibrium between the growth medium and the bulk crystal, F is the surface enrichment factor and l (0.5 nm) is the half-thickness of the enriched surface layer. The values of F values were set as 6 and 0.3 for Sr and Mg, respectively. The enrichment factor (F) was taken as the ratio of maximum measured Sr ($Sr_{surface}$) or minimum measured Mg ($Mg_{surface}$) concentration to their assumed lattice equilibrium values (Me_{eq}).

The diffusivity of Sr in the calcite lattice (D_l^{Sr}) was extrapolated from high temperature data of Cherniak (1997) as ~10^{-18} nm^2/s. Two experimental studies on diffusion of Mg in calcite lattice yielded controversial results (Fisler and Cygan, 1999; Kent et al., 2001). The extrapolation of their high temperature data to 25 °C yielded D_l^{Mg} values of 10^{-35} and $5 \cdot 10^{-12}$ nm^2/s, respectively. Therefore, in our study we assumed that diffusivities of Sr and Mg in the calcite surface distinct layer are similar ($D_s^{Mg} \approx D_s^{Sr}$). The value of D_l is not as important in the model as soon as $D_l \ll D_s$. For example at V = 0.1 nm/s changing of D_l from 10^{-18} to 10^{-35} affects K^{Me}/K_{eq}^{Me} by less than 2%.

The parameters of D_s and distance multiplier (m) were optimized for obtaining the best fit for the experimental Sr data, i.e. $D_s = 0.1$ and $m = \infty$. Here, infinite m means that the diffusivity is independent of depth in the crystal (and equal to D_s) over a distance much greater than the thickness of the compositionally distinct near-surface layer. For comparison of GEM parameters that were used in this study and other works please see Table A1.

Table A1
Parameters used in GEM calculations for the data from this study and other works at 25 °C.

Element in calcite	K_{eq}	F	D_l (nm^2/s)	D_s (nm^2/s)	l (nm)	m	Reference
Magnesium	0.035	0.3	~10^{-18}	0.1	0.5	∞	This work
Strontium	0.045	6	~10^{-18}	0.1	0.5	∞	This work
Strontium	0.02	14	~10^{-18}	0.06	0.5	∞	Combined data
Strontium[a]	0.02	12.5	~10^{-18}	0.06	0.5	8	Tang et al. (2008)
Strontium[b]	0.02	10	~10^{-18}		0.5		Stoll et al. (2002b)

K_{eq} = 0.02 correspond to the data of Tesoriero and Pankow (1996).
[a] Fitting experimental data of Tang et al. (2008).
[b] Fitting experimental data of Lorens (1981) and Tesoriero and Pankow (1996).

Appendix 3. Supplementary data

Supplementary data to this article can be found online at http://dx.doi.org/10.1016/j.chemgeo.2013.12.019.

References

Allison, N., 1996. Comparative determinations of trace and minor elements in coral aragonite by ion microprobe analysis, with preliminary results from Phuket, southern Thailand. Geochim. Cosmochim. Acta 60, 3457–3470.

Anand, P., Elderfield, H., 2005. Variability of Mg/Ca and Sr/Ca between and within the planktonic foraminifers *Globigerina bulloides* and *Globorotalia truncatulinoides*. Geochem. Geophys. Geosyst. 6 (11). http://dx.doi.org/10.1029/2004GC000811.

Baker, A., Genty, D., Dreybrodt, W., Barnes, W.L., Mockler, N.J., Grapes, J., 1998. Testing theoretically predicted stalagmite rate with recent annually laminated samples: implications for past stalagmite deposition. Geochim. Cosmochim. Acta 62, 393–404.

Bentov, S., Erez, E., 2005. Novel observations on biomineralization processes in foraminifera and implications for Mg/Ca ratio in the shells. Geology 33, 841–844. http://dx.doi.org/10.1130/G21800.1.

Bentov, S., Erez, E., 2006. Impact of biomineralization processes on the Mg content of foraminiferal shells: a biological perspective. Geochem. Geophys. Geosyst. 7 (1), Q01P08. http://dx.doi.org/10.1029/2005GC001015.

Bice, K.L., Layne, G.D., Dahl, K.A., 2005. Application of secondary ion mass spectrometry to the determination of Mg/Ca in rare, delicate, or altered planktonic foraminifera: examples from the Holocene, Paleogene, and Cretaceous. Geochem. Geophys. Geosyst. 6 (12), Q12P07. http://dx.doi.org/10.1029/2005GC000974.

Bleuzen, A., Pittet, P.A., Helm, L., Merbach, A.E., 1997. Water exchange on magnesium(II) in aqueous solution: a variable temperature and pressure ^{17}O NMR study. Magn. Reson. Chem. 35, 765–773.

Branson, O., Redfern, S.A.T., Tyliszczak, T., Sadekov, A., Langer, G., Kimoto, K., Elderfield, H., 2013. The coordination of Mg in foraminiferal calcite. Earth Planet. Sci. Lett. 383, 134–141.

Cherniak, D.J., 1997. An experimental study of strontium and lead diffusion in calcite, and implications for carbonate diagenesis and metamorphism. Geochim. Cosmochim. Acta 61, 4173–4179.

Cleroux, et al., 2008. Mg/Ca and Sr/Ca ratios in planktonic foraminifera: proxies for upper water column temperature reconstruction. Paleoceanography 23. http://dx.doi.org/10.1029/2007PA001505.

Cruz Jr., F.W., et al., 2007. Evidence of rainfall variations in Southern Brazil from trace element ratios (Mg/Ca and Sr/Ca) in a Late Pleistocene stalagmite. Geochim. Cosmochim. Acta 71, 2250–2263.

de Villiers, S., Greaves, M., Elderfield, H., 2002. An intensity ratio calibration method for the accurate determination of Mg/Ca and Sr/Ca of marine carbonates by ICP-AES. Geochem. Geophys. Geosyst. 3. http://dx.doi.org/10.1029/2001GC000169 (issn: 1525-2027).

Dekens, P.S., Lea, D.W., Pak, D.K., Spero, H.J., 2002. Core top calibration of Mg/Ca in tropical foraminifera: refining paleotemperature estimation. Geochem. Geophys. Geosyst. 3. http://dx.doi.org/10.1029/2001GC000200.

Denniston, R.F., Shearer, C.K., Layne, G.D., Vaniman, D.T., 1997. SIMS analyses of minor and trace elements distributions in fracture calcite form Yucca Mountains, Nevada, USA. Geochim. Cosmochim. Acta 61, 1803–1818.

Eggins, S.M., Sadekov, A., De Deckker, P., 2004. Modulation and daily banding of Mg/Ca in *Orbulina universa* tests by symbiont photosynthesis and respiration: a complication for seawater thermometry? Earth Planet. Sci. Lett. 225, 411–419.

Elderfield, H., Bertram, C.J., Erez, J., 1996. A biomineralization model for the incorporation of trace elements into foraminiferal calcium carbonate. Earth Planet. Sci. Lett. 142, 409–423.

Elderfield, H., Vautravers, M., Cooper, M., 2002. The relationship between shell size and Mg/Ca, Sr/Ca, δ^{18}O, and δ^{13}C of species of planktonic foraminifera. Geochem. Geophys. Geosyst. 3, 8. http://dx.doi.org/10.1029/2001GC000194.

Erez, J., 2003. The source of ions for biomineralization in foraminifera and their implications for paleoceanographic proxies. In: Dove, P.M., DeYoreo, J.J., Weiner, S. (Eds.), Rev. Mineral. Geochem. (Biomineralization), 54, pp. 115–149.

Fenter, P., Geissbuhler, P., Dimasi, E., Srajer, J., Sorensen, L.B., Sturchio, N.C., 2000. Surface speciation of calcite observed in situ by high-resolution X-ray reflectivity. Geochim. Cosmochim. Acta 64, 1221–1228.

Filipsson, H.L., Bernhard, J.M., Lincoln, S.A., McCorkle, D.C., 2010. A culture-based calibration of benthic foraminiferal paleotemperature proxies: delta O-18 and Mg/Ca results. Biogeosciences 7, 1335–1347.

Finch, A.A., Allison, N., 2007. Coordination of Sr and Mg in calcite and aragonite. Mineral. Mag. 71 (5), 539–552.

Fisler, D.K., Cygan, R.T., 1999. Diffusion of Ca and Mg in calcite. Am. Mineral. 84, 1392–1399.

Freitas, P.S., Clarke, L.J., Kennedy, H., Richardson, C.A., 2008. Inter- and intra-specimen variability masks reliable temperature control on shell Mg/Ca ratios in laboratory- and field-cultured *Mytilus edulis* and *Pecten maximus* (bivalvia). Biogeosciences 5, 1245–1258.

Freitas, P.S., Clarke, L.J., Kennedy, H., Richardson, C.A., 2009. Ion microprobe assessment of the heterogeneity of Mg/Ca, Sr/Ca and Mn/Ca ratios in *Pecten maximus* and *Mytilus edulis* (bivalvia) shell calcite precipitated at constant temperature. Biogeosci. Discuss. 6, 1267–1316.

Gabitov, R.I., 2005. Partitioning of Sr, Mg, U, ^{18}O/^{16}O, and ^{13}C/^{12}C Between Calcium Carbonate Minerals and Fluid at Different Temperatures and Crystal Growth Rates. (PhD Thesis) Rensselaer Polytechnic Institute.

Gabitov, R.I., 2010. Partitioning of Sr, Mg, U, ^{18}O/^{16}O, and ^{13}C/^{12}C Between Calcium Carbonate Minerals and Fluid at Different Temperatures and Crystal Growth Rates. VDM Verlag Dr. Müller e.K 124.

Gabitov, R.I., 2013. Growth-rate induced disequilibrium of oxygen isotopes in aragonite: an in situ study. Chem. Geol. 351, 268–275.

Gabitov, R.I., Watson, E.B., 2006. Partitioning of strontium between calcite and fluid. Geochem. Geophys. Geosyst. 7, Q11004. http://dx.doi.org/10.1029/2005GC001216.

Gabitov, R.I., Gaetani, G.A., Watson, E.B., Cohen, A.L., Ehrlich, H.L., 2008. Experimental determination of temperature and growth rate effects on U^{6+} and Mg^{2+} partitioning between aragonite and fluid. Geochim. Cosmochim. Acta 72, 4058–4068.

Gabitov, R.I., Schmitt, A.K., Rosner, M., McKeegan, K.D., Gaetani, G.A., Cohen, A.L., Watson, E.B., Harrison, T.M., 2011. In situ δ^7Li, Li/Ca, and Mg/Ca analyses of synthetic aragonites. Geochem. Geophys. Geosyst. 12, Q03001. http://dx.doi.org/10.1029/2010GC003322.

Gabitov, R.I., Watson, E.B., Sadekov, A., 2012. Oxygen isotope fractionation between calcite and fluid as a function of growth rate and temperature: an in situ study. Chem. Geol. 306–307, 92–102.

Gabitov, R.I., Gagnon, A.C., Guan, Y., Eiler, J.M., Adkins, J.F., 2013. Accurate Mg/Ca, Sr/Ca, and Ba/Ca ratios measurements in carbonates by SIMS and NanoSIMS and an assessment of heterogeneity in common calcium carbonate standards. Chem. Geol. 356, 94–108.

Gaetani, G.A., Cohen, A.L., 2006. Element partitioning during precipitation of aragonite from seawater: a framework for understanding paleoproxies. Geochim. Cosmochim. Acta 70, 4617–4634.

Greaves, M., Barker, S., Daunt, C., Elderfield, H., 2005. Accuracy, standardization, and interlaboratory calibration standards for foraminiferal Mg/Ca thermometry. Geochem. Geophys. Geosyst. 6, Q02D13. http://dx.doi.org/10.1029/2004GC000790.

Greaves, M., et al., 2008. Interlaboratory comparison study of calibration standards for foraminiferal Mg/Ca thermometry. Geochem. Geophys. Geosyst. 9, Q08010. http://dx.doi.org/10.1029/2008GC001974.

Griffiths, et al., 2010. Evidence for Holocene changes in Australian–Indonesian monsoon rainfall from stalagmite trace element and stable isotope ratios. Earth Planet. Sci. Lett. 292, 27–38.

Gruzensky, P.M., 1967. Growth of calcite crystals. J. Phys. Chem. Solids S1, 365–367.

Hart, S.R., Cohen, A.L., 1996. An ion probe study of annual cycles of Sr/Ca and other trace elements in corals. Geochim. Cosmochim. Acta 60, 3075–3084.

Hartley, G., Mucci, A., 1996. The influence of PCO_2 on the partitioning of magnesium in calcite overgrowths precipitated from artificial seawater at 25° and 1 atm total pressure. Geochim. Cosmochim. Acta 60, 315–324.

Hathorne, E., et al., 2013. Inter-laboratory study for coral Sr/Ca and other element/Ca ratio measurements. Geochem. Geophys. Geosyst. 14. http://dx.doi.org/10.1002/ggge.20230.

Herzog, R.F.K., Poschenrieder, W.P., Satkiewicz, F.G., 1973. Observation of clusters in a sputtering ion source. Radiat. Eff. 18, 199–205.

Holcomb, M., Cohen, A.L., Gabitov, R.I., Hutter, J.L., 2009. Compositional and morphological features of aragonite precipitated experimentally from seawater and biogenically by corals. Geochim. Cosmochim. Acta 73, 4166–4179.

Holland, H.D., Holland, H.J., Munoz, J.L., 1964. The coprecipitation of cations with $CaCO_3$-II. The coprecipitation of Sr with calcite between 90 and 100 °C. Geochim. Cosmochim. Acta 28, 1287–1301.

Huang, Y., Fairchild, I.J., 2001. Partition of Sr^{2+} and Mg^{2+} into calcite under karst-analogue experimental conditions. Geochim. Cosmochim. Acta 65, 47–62.

Immenhauser, A., Nagler, T.F., Steuber, T., Hippler, D., 2005. A critical assessment of mollusk $^{18}O/^{16}O$, Mg/Ca, and $^{44}Ca/^{40}Ca$ ratios as proxies for Cretaceous seawater temperature seasonality. Palaeogeogr. Palaeoclimatol. Palaeoecol. 215, 221–237.

Johnson, K.M., Wills, K.D., Butler, D.B., Johnson, W.K., Wong, C.S., 1993. Coulometric total carbon dioxide analysis for marine studies, maximizing the performance of an automated gas extraction system and coulometric detector. Mar. Chem. 44, 167–187.

Katz, A., 1973. The interaction of magnesium with calcite during crystal growth at 25–90 °C and one atmosphere. Geochim. Cosmochim. Acta 37, 1563–1586.

Kent, A.J.R., Hutcheon, I.D., Ryerson, F.J., Phinney, D.L., 2001. The temperature of formation of carbonate in Martian meteorite ALH84001: constraints from cation diffusion. Geochim. Cosmochim. Acta 65, 311–321.

Kunioka, D., Shirai, K., Takahata, N., Sano, Y., 2006. Microdistribution of Mg/Ca, Sr/Ca, and Ba/Ca ratios in *Pulleniatina obliquiloculata* test by using a NanoSIMS: implication for the vital effect mechanism. Geochem. Geophys. Geosyst. 7, Q12P20. http://dx.doi.org/10.1029/2006GC001280.

Lanzillo, N.A., Watson, E.B., Thomas, J.B., Nayak, S.K., Curioni, A., 2014. Near-surface controls on the composition of growing crystals: Car-Parrinello molecular dynamics (CPMD) simulations of Ti energetics and diffusion in alpha quartz. Geochim. Cosmochim. Acta (in press).

Lea, D.W., Mashiotta, T.A., Spero, H.J., 1999. Control of magnesium and strontium uptake in planktonic foraminifera determined by live culturing. Geochim. Cosmochim. Acta 63, 2369–2379.

Lewis, E., Wallace, D.W.R., 1998. Program Developed for CO_2 System Calculations. ORNL/CDIAC-105 Carbon Dioxide Information Analysis Center, Oak Ridge National Laboratory, U.S. Department of Energy, Oak Ridge, Tennessee.

Li, Y.-H., Gregory, S., 1974. Diffusion of ions in sea water and in deep-sea sediments. Geochim. Cosmochim. Acta 38, 703–714.

Lincoln, S.F., Merbach, A.E., 1995. Substitution reactions of solvated metal ions. In: Sykes, A.G. (Ed.), Advances in Inorganic Chemistry, 42, pp. 1–88.

Lorens, R.B., 1981. Sr, Cd, Mn, and Co distribution coefficients in calcite as a function of calcite precipitation rate. Geochim. Cosmochim. Acta 45, 553–561.

Martin, P.A., Lea, D.W., Mashiotta, T.A., Papenfuss, T., Sarnthein, M., 1999. Variation of foraminiferal Sr/Ca over Quaternary glacial–interglacial cycles: evidence for changes in mean ocean Sr/Ca? Geochem. Geophys. Geosyst. 1 (paper no. 1999GC000006).

Mavromatis, V., Gautier, Q., Bosc, O., Schott, J., 2013. Kinetics of Mg partition and Mg stable isotope fractionation during its incorporation in calcite. Geochim. Cosmochim. Acta 114, 188–203.

McCorkle, D.C., Martin, P.A., Lea, D.W., Klinkhammer, G.P., 1995. Evidence of a dissolution on benthic foraminiferal shell chemistry: $\delta^{13}C$, Cd/Ca, Ba/Ca, and Sr/Ca results from the Ontong Java Plateau. Paleoceanography 10, 699–714.

Millero, F.J., 1995. Thermodynamics of the carbon dioxide system in the oceans. Geochim. Cosmochim. Acta 59, 661–677.

Morse, J.W., Wang, Q., Tsio, M.Y., 1997. Influences of temperature and Mg:Ca ratio on $CaCO_3$ precipitates from seawater. Geology 25, 85–87.

Mortyn, P.G., Elderfield, H., Anand, P., Greaves, M., 2005. An evaluation of controls on planktonic foraminiferal Sr/Ca: comparison of water column and core-top data from a North Atlantic transect. Geochem. Geophys. Geosyst. 6, Q12007. http://dx.doi.org/10.1029/2005GC001047.

Mucci, A., 1983. The solubility of calcite and aragonite in seawater at various salinities, temperatures, and one atmosphere total pressure. Am. J. Sci. 28 (1), 780–799.

Mucci, A., 1987. Influence of temperature on the composition of magnesian calcite overgrowths precipitated from seawater. Geochim. Cosmochim. Acta 51, 1977–1984.

Mucci, A., Morse, J.W., 1983. The incorporation of Mg^{2+} and Sr^{2+} into calcite overgrowths: influences of growth rate and solution composition. Geochim. Cosmochim. Acta 47, 217–233.

Nehrke, G., Reichart, G.J., Van Cappellen, P., Meile, C., Bijma, J., 2007. Dependence of calcite growth rate and Sr partitioning on solution stoichiometry: non-Kossel crystal growth. Geochim. Cosmochim. Acta 71, 2240–2249.

Nurnberg, D., Bijma, J., Hemleben, C., 1996. Assessing the reliability of magnesium in foraminiferal calcite as a proxy for water mass temperatures. Geochim. Cosmochim. Acta 60, 2483.

Owen, R., Kennedy, H., Richardson, C., 2002. Isotopic partitioning between scallop shell calcite and seawater: effect of shell growth rate. Geochim. Cosmochim. Acta 66, 1727–1737.

Paquette, J., Reeder, R.J., 1995. Relationship between surface structure, growth mechanism, and trace element incorporation in calcite. Geochim. Cosmochim. Acta 59, 735–749.

Pavlov, M., Siegbahn, P.E.M., Sandstro, M., 1998. Hydration of beryllium, magnesium, calcium, and zinc ions using density functional theory. J. Phys. Chem. A 102, 219–228.

Raitzsch, M., Duenas-Bohorquez, A., Reichart, G.-J., de Nooijer, L.J., Bickert, T., 2010. Incorporation of Mg and Sr in calcite of cultured benthic foraminifera: impact of calcium concentration and associated calcite saturation state. Biogeosciences 7, 869–881.

Reeder, R.J., Grams, J.C., 1987. Sector zoning in calcite cement crystals: implications for trace element distributions in carbonates. Geochim. Cosmochim. Acta 51, 187–194.

Rickaby, R.E.M., Schrag, D.P., Zondervan, I., Riebesell, U., 2002. Growth rate dependence of Sr incorporation during calcification of *Emiliania huxleyi*. Global Biogeochem. Cycles 16, 1006. http://dx.doi.org/10.1029/2001GB001408.

Rodriguez-Cruz, S.E., Jockusch, R.A., Williams, E.R., 1999a. Binding energies of hexahydrated alkaline earth metal ions, $M^{2+}(H_2O)_6$, M = Mg, Ca, Sr, Ba: evidence of isomeric structures for magnesium. J. Am. Chem. Soc. 121, 1986–1987.

Rodriguez-Cruz, S.E., Jockusch, R.A., Williams, E.R., 1999b. Hydration energies and structures of alkaline earth metal ions, $M^{2+}(H_2O)_n$, n = 5–7, M = Mg, Ca, Sr, and Ba. J. Am. Chem. Soc. 121, 8898–8906.

Rosenthal, Y., Boyle, E.D., Slowey, N., 1997. Temperature control on the incorporation of magnesium, strontium, fluorine, and cadmium into benthic foraminiferal shells from Little Bahama Bank: prospects for thermocline paleoceanography. Geochim. Cosmochim. Acta 61, 3633–3643.

Rosenthal, Y., et al., 2004. Interlaboratory comparison study of Mg//Ca and Sr//Ca measurements in planktonic foraminifera for paleoceanographic research. Geochem. Geophys. Geosyst. 5 (4), Q04D09. http://dx.doi.org/10.1029/2003GC000650.

Sadekov, A., Eggins, S.M., De Deckker, P., 2005. Characterization of Mg/Ca distributions in planktonic foraminifera species by electron microprobe mapping. Geochem. Geophys. Geosyst. 6, Q12P06. http://dx.doi.org/10.1029/2005GC000973.

Sadekov, A., Eggins, Stephen M., Klinkhammer, Gary P., Rosenthal, Yair, 2010. Effects of seafloor and laboratory dissolution on the Mg/Ca composition of *Globigerinoides sacculifer* and *Orbulina universa* tests—a laser ablation ICPMS microanalysis perspective. Earth Planet. Sci. Lett. 292, 312–324.

Saulnier, S., Rollion-Bard, C., Vigier, N., Chaussidon, M., 2012. Mg isotope fractionation during calcite precipitation: an experimental study. Geochim. Cosmochim. Acta 91, 75–91.

Schott, J., Pokrovsky, O.S., Oelkers, E.H., 2009. The link between mineral dissolution/precipitation kinetics and solution chemistry. Rev. Mineral. Geochem. 70, 207–258.

Segev, E., Erez, J., 2006. Effect of Mg/Ca ratio in seawater on shell composition in shallow benthic foraminifera. Geochem. Geophys. Geosyst. 7, Q02P09. http://dx.doi.org/10.1029/2005GC000969.

Shimizu, N., Semet, M.P., Allegre, C.J., 1978. Geochemical applications of quantitative ion-microprobe analysis. Geochim. Cosmochim. Acta 42, 1321–1334.

Smith, V.G., Tiller, W.A., Rutter, J.W., 1955. A mathematical analysis of solute redistribution during solidification. Can. J. Phys. 33, 723–745.

Stack, A.G., Grantham, M.C., 2010. Growth rate of calcite steps as a function of aqueous calcium-to-carbonate ratio: independent attachment and detachment of calcium and carbonate ions. Cryst. Growth Des. 10, 1409–1413.

Stephenson, A.E., DeYoreo, J.J., Wu, L., Wu, K.J., Hoyer, J., Dove, P.M., 2008. Peptides enhance magnesium signature in calcite: insights into origins of vital effects. Science 322, 724–727.

Stipp, S.L., Hochella Jr., M.F., Parks, G.A., Leckie, J.O., 1992. Cd^{2+} uptake by calcite, solid-state diffusion, and the formation of solid-solution: interface process observed with near-surface sensitive techniques (XPS, LEED, and AES). Geochim. Cosmochim. Acta 56, 1941–1954.

Stoll, H.M., Schrag, D.P., 2000. Coccolith Sr/Ca as a new indicator of coccolithophorid calcification growth rate. Geochem. Geophys. Geosyst. 1 (1999GC000015).

Stoll, H.M., Klaas, C., Probert, I., Encinar, J.R., Garcia Alonso, J.I., 2002a. Calcification rate and temperature effects on Sr partitioning in coccoliths of multiple species of coccolithophorids in culture. Glob. Planet. Chang. 34, 153–171.

Stoll, H.M., Rosenthal, Y., Falkowski, P., 2002b. Climate proxies from Sr/Ca of coccolith calcite: calibrations from continuous culture of *Emiliania huxleyi*. Geochim. Cosmochim. Acta 66, 927–936.

Tang, J., Köhler, S.J., Dietzel, M., 2008. Sr^{2+}/Ca^{2+} and $^{44}Ca/^{40}Ca$ fractionation during inorganic calcite formation: I. Sr incorporation. Geochim. Cosmochim. Acta 72, 3718–3732.

Tang, J., Niedermayr, A., Köhler, S.J., Böhm, F., Kisakürek, B., Eisenhauer, A., Dietzel, M., 2012. Sr^{2+}/Ca^{2+} and $^{44}Ca/^{40}Ca$ fractionation during inorganic calcite formation: III. Impact of salinity/ionic strength. Geochim. Cosmochim. Acta 77, 432–443.

ter Kuile, B., Erez, J., 1984. In situ growth rate experiments on the symbiotic-bearing foraminifera. *Amphisteginalobifera* and *Amphisorushemprichii*. J. Foramineferal Res. 14, 262–276.
Tesoriero, A.J., Pankow, J.F., 1996. Solid solution partition of Sr^{2+}, Ba^{2+}, and Cd^{2+} to calcite. Geochim. Cosmochim. Acta 60, 1053–1063.
Wasylenki, L.E., Dove, P.M., Wilson, D.S., De Yoreo, J.J., 2005. Nanoscale effects of strontium on calcite growth: an in situ AFM study in the absence of vital effects. Geochim. Cosmochim. Acta 69, 3017–3027.
Watson, E.B., 1996. Surface enrichment and trace-element uptake during crystal growth. Geochim. Cosmochim. Acta 60, 5013–5020.
Watson, E.B., 2004. A conceptual model for near-surface kinetic controls on the trace-element and stable isotope composition of abiogenic calcite crystals. Geochim. Cosmochim. Acta 68, 1473–1488.
Watson, E.B., Liang, Y., 1995. A simple model for sector zoning in slowly growing crystals: implications for growth rate and lattice diffusion, with emphasis on accessory minerals in crustal rocks. Am. Mineral. 80, 1179–1187.
Watson, E.B., Müller, T., 2009. Non-equilibrium isotopic and elemental fractionation during diffusion-controlled crystal growth under static and dynamic conditions. Chem. Geol. 267, 111–124.